Droplet Detachment Mechanism in a High-Speed Gaseous Microflow

Brian Carroll

Carlos Hidrovo[1]
e-mail: hidrovo@mail.utexas.edu

The University of Texas at Austin,
Multiscale Thermal Fluids Laboratory,
Austin, TX 78712

This paper experimentally investigates the mechanism of water droplet detachment in a confined microchannel under highly inertial ($10 < Re < 200$) air flow conditions. Experimental observations show that as the Reynolds number of the continuous phase is increased, the droplet transitions from an elongated slug to a nearly uniform aspect ratio droplet. Supporting scaling arguments are then made that examine the relevant forces induced by the continuous phase on the droplet at the point of detachment. The inertial, viscous, and hydrodynamic pressure forces that result as the air flow is confined in the small gap between droplet and channel walls are compared to the surface tension force pinning the droplet at the injection site. The results indicate that the dominant detachment mechanism transitions from the hydrostatic pressure difference to inertial drag as the continuous phase velocity is increased. [DOI: 10.1115/1.4024057]

Introduction

One of the most important droplet-based microfluidic operations is the droplet generation and entrainment process. For the high throughput capability required by the next generation of multifunctional microfluidic devices, rapid and controllable droplet formation is paramount. The Reynolds (Re) number is almost always less than unity in traditional oil-water droplet-based systems due to the highly viscous continuous phase oil. As such, the detachment process is overwhelmingly governed by the interaction between viscous and surface tension forces that lead to a well characterized Capillary (Ca) number dependence [1–4]. This balance produces well-defined droplets or slugs that inevitably lack any trailing tail features or liquid film development. This is a direct result of the surface energy of the discrete phase relative to the continuous phase which provides droplet formation and transport without direct contact with the channel walls. The continuous phase provides lubrication during transport and there always remains a thin continuous phase film separating the droplet from the channel walls. The images shown in Fig. 1 provide visual confirmation of the different detachment characteristics for oil-liquid versus gas-liquid flows in a microfluidic T-junction. In high speed (>1 m/s) gas-liquid droplet flows, the picture is much different, and to date, not well defined. Formation of liquid droplets under a high speed gas flow displays a new realm of force interactions because the inertia that would normally be neglected in oil-based flows becomes an important driving force. Additionally, the surface tension of the liquid phase also increases with incorporation of a gaseous flow. These richer dynamics lead to unusual liquid topology, which can range between asymmetrical droplets, long trailing tail slugs, thin films, and free-surface stratified flow.

Generating droplets from a continuous liquid supply stream is not a new endeavor. With the exception of early inquiry by Plateau [5], Savart [6], and Rayleigh [7,8], technical progress and scientific understanding of droplet breakup is historically application driven. Landmark examples include agricultural fertilization, liquid fuel propulsion, and pharmaceutical development. Atomizing a liquid is a simple process. All that is required is a large velocity difference between the liquid to be atomized and the surrounding environment. This is accomplished by forcing a liquid stream through a small orifice using a large pressure difference. This straightforward method for generating droplet sprays works well in fuel injectors and paint sprayers, where precise individual droplet size control is not required. However, generation of monodisperse droplets is significantly more difficult. In the 1970s, when ink jet printing technology was in its infancy, linear and nonlinear perturbation analyses became commonplace in an effort to understand, predict, and suppress a common problem in circular jet breakup: satellite drop formation [9]. The resurgence of research and development during the past decade has largely been facilitated by the burgeoning microfluidic sciences, where droplet based architectures have quickly replaced continuous flow systems.

Gas-liquid droplet microchannel flows offer opportunities to mix different reactants with increased through-put and reduced mixing times. By colliding two droplets at a common channel junction, mixing takes place under highly inertial conditions as opposed to mixing dominated by mass diffusion. Furthermore, using a gaseous phase for droplet generation and transport offers the benefits of reduced pressure requirements in comparison to liquid-liquid flows with the same volumetric flow rates. To date, inertia-based, gas-liquid micromixing devices have not been fully realized under laboratory conditions due to a lack of understanding of the droplet generation and collision process when the two phases differ significantly. Droplet collisions in unconfined flows, however, have been studied extensively for a number of decades [10–12]. Droplet collision at low velocity was investigated by Wang et al. [13] and on a single interface surface by Aryafar and Kavehpour [14]. The presence of a wall, or walls, introduces added complexity and the resultant collision outcome—droplet coalescence, separation, or bounce—is difficult to predict. Droplet collision in two phase liquid-liquid microchannel flows was examined by Graaf et al. [2] and Christopher et al. [15], but the process has not been fully mapped for confined microchannel flows. Adding two different immiscible phases with considerably different properties, such as air and water, adds to the complexity even further.

Before droplet collision occurs, each droplet must first be detached and entrained into a high speed gas flow. Generating monodisperse droplets of known volume and geometry is a prerequisite to droplet collisions and therefore the detachment process must be well understood and characterized. The detachment process was investigated numerically by Zhu et al. [16] and experimentally by Carroll and Hidrovo [17] and Sugiura et al. [18]; however, to date the detachment mechanism remains unclear. This paper experimentally investigates the droplet detachment process in a gaseous microflow with continuous phase velocities in excess of 1 m/s using a T-junction configuration. The objective

[1]Corresponding author.

Contributed by the Fluids Engineering Division of ASME for publication in the JOURNAL OF FLUIDS ENGINEERING. Manuscript received Juy 27, 2012; final manuscript received March 14, 2013; published online May 17, 2013. Assoc. Editor: Ali Beskok.

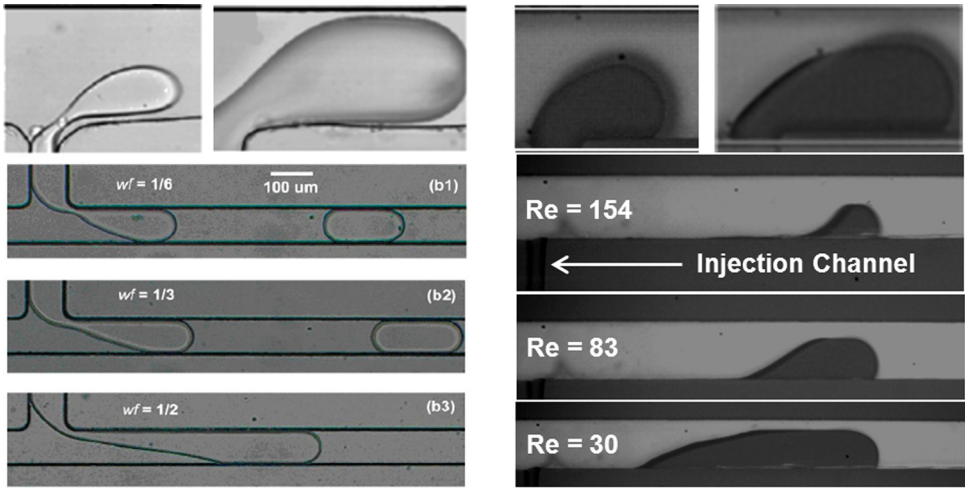

Fig. 1 Water droplets detaching into oil flow (upper left) and changes in water droplet size for increasing water to oil flow rate ratios (lower left) [20]. Note that a thin oil film separates the droplet from the channel walls. Water droplet detaching into gaseous flow (upper right) and changes in water droplet size for decreasing gas Re number (lower right). Even for small air Re numbers, the detached droplet never fills the channel width as compared to the oil-based flow and is in direct contact with the channel walls.

is to gain an understanding of the parameters governing droplet detachment and resulting detached droplet shape. The required liquid flow rates ($\sim$1 μL/min) and gas flow rates ($\sim$10 sccm) required to form and detach liquid droplets at a T-junction was facilitated using multiphase microfluidic test bed. The detached droplet is visualized through the use of a high speed camera and the resulting images are analyzed for droplet size information. First order scaling arguments are then made to qualitatively assess the measurements and observations of the experiments. The results indicate that droplet detachment at $\mathrm{Re}_{Dh} < 100$ is driven by pressure differences across the droplet as opposed to viscous shearing stresses. The pressure difference provides the force necessary to overcome the surface tension force at the droplet-wall interface. For $\mathrm{Re}_{Dh} > 100$, the detachment mechanism transitions pressure induced to inertial drag.

Device Fabrication

To study the droplet formation and detachment mechanisms, a standard T-junction configuration was designed where the gas flow is normal to the liquid injection site. The channel length leading up to the injection site provided fully developed conditions at the liquid injection site under the range of gas velocities considered. Sufficient length ($\sim$50 hydraulic diameters) was added past the injection site such that the droplet growth and detachment process occurs unhindered by downstream channel features. Four millimeter plenums were added to the air and liquid inlets to facilitate the introduction of gas and liquid tubing ports. Figure 2 shows a typical device used for droplet detachment and collision studies.

The microfabrication process used to fabricate the droplet detachment device was based on conventional, 2D soft lithography techniques and used polydimethylsiloxane (PDMS) as the substrate material. The process flow shown in Fig. 3 depicts the major fabrication steps. The process begins by creating a negative mold of the microchannel geometry on a standard 4″ diameter, 500 μm thick silicon wafer using photolithography. The wafer is cleaned and prepared using standard cleaning procedures. A negative near UV resist (SU8-2050 MicroChem Corp.) is spin coated onto the wafer to a thickness dictated by the microchannel depth. The coated wafer is then baked to remove the solvents in the resist. Once cured, the wafer is placed in a mask aligner and exposed to 392 nm radiation through a mask containing the microchannel image. Since the

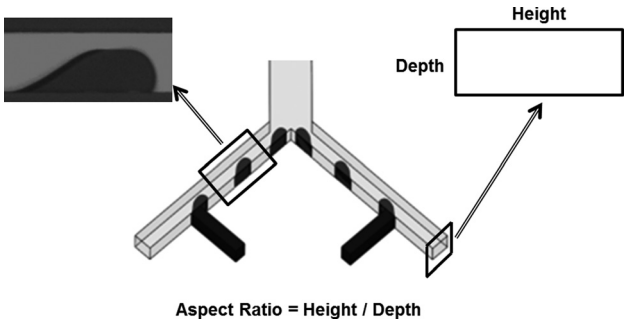

Fig. 2 CAD image (not to scale) of the gas-liquid microfluidic device used for droplet detachment and droplet collisions studies. Four different devices were tested with the following aspect ratio: 1.75, 2.0, 2.0, and 4.25.

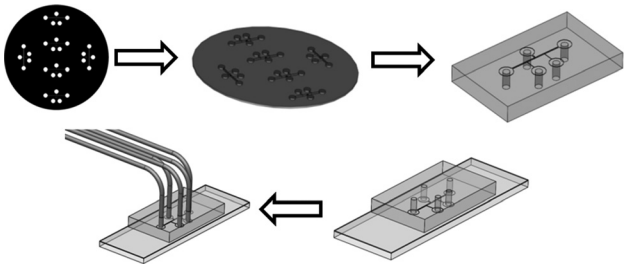

Fig. 3 Process flow for PDMS soft lithography: mask CAD design, photolithography, molding, bonding, and fluid and gas port integration

smallest feature size on the microchannel is typically 15 μm, 7 mil transparency film mask is used as an alternative to a chromium mask. The exposed wafer is then developed using the appropriate developer solution and baked at the prescribed temperature and duration.

Once the photolithography process is complete, the resist-coated wafer is treated with trichlorosilane in a reduced pressure environment for approximately 4 h. This process renders the silicon surface hydrophobic and facilitates mold release. The PDMS

solution is prepared using Sylgard 184 silicone elastomer base mixed with a curing agent at a 5:1 weight ratio. Unlike the 10:1 ratio recommended by the manufacturer, the increase curing agent produces finished devices that are significantly more rigid. The PDMS solution is poured onto silicon mold and the assembly is placed in a vacuum desiccator to remove trapped air bubbles and promote solvent vaporization. The assembly is then placed on a hot plate in ambient surroundings and baked at 65 °C for approximately 3–6 h. Once cured, the PDMS is peeled from the silicon substrate.

The available real estate on a 4″ silicon wafer allows a number of devices to be created in a single soft lithography process. Each device is cut from the PDMS mold and prepared for fluid and gas porting. A 2 mm diameter belt-hole puncher is used to core the PDMS device at each gas and fluid inlet and outlet. Each device is then cleaned with methanol and prepared for bonding. A $1'' \times 3''$ standard microscope slide is spin coated with a ~5 mm thick layer of PDMS using a 10:1 weight ratio. The glass slide provides a rigid substrate to support each device to and allows bottom up visualization using an inverted microscope. The uncured slides are placed in the vacuum desiccator for 1 h and then placed on a hot plate at 55 °C. Before the PDMS is fully cured, a clean device is carefully placed on its surface. The combination of different mixing ratios promotes diffusion between the device and substrate resulting in a permanent bond that is stronger than any other PDMS to PDMS bonding technique. Pressures in excess of 20 psi have been introduced into these devices without failure.

Experimental Setup

The quality and confidence of any result obtained by experiment is greatly sensitive to the measurement techniques and equipment employed. Starting from the ground up, a custom microfluidic test bed has been designed for experimental investigation of multiphase flows, particularly high speed gas-liquid droplet flows. The test bed is capable of providing gas flow control from 10^{-8} to 10^{-6} m^3/s with 10^{-9} m^3/s precision (0.5 to 100 sccm with 0.05 sccm). This is accomplished using a voltage-controlled pressure regulator (Proportion-Air QPV1) with pressure transducer feedback control. Flow rates are measured using thermal mass flow sensors (Sierra Smart-Trak2). For tests where air is used as the continuous phase, facility supplied compressed air is first dried in a desiccant chamber and cleaned using 0.2 μm filters. A rough pressure regulator is used to reduce the facility pressure before routing the air flow into a delivery manifold. Individual and multiple air streams are activated using the voltage-controlled pressure regulators. A hardware diagram of the test bed is shown in Fig. 4.

Liquid flow control is provided by a custom pressurized liquid reservoir and fast switching solenoid valve (Parker–Series 3). This arrangement was designed for droplet generation purposes where the feature of utmost importance is flow stability. The workhorse for microfluidic liquid delivery is typically a constant displacement pump. These types of pumps are inherently unstable in terms of pressure response. For gas-liquid droplet generation, there is no viscous continuous phase to dampen these instabilities and the effects become amplified. The result is unpredictable droplet sizes and unsteady generation rates that show multiple frequency contents. The solenoid valve can be used with frequencies between 0.05 to 40 Hz and duty cycles from 5 to 95%. The resulting liquid flow rate can then be delivered with precision by changing the reservoir pressure, switching frequency, and duty cycle, thereby providing complete control over liquid delivery into the microfluidic device. The liquid solenoid valves were powered using a 24 V DC power supply and controlled using a delay generator (Stanford Research DG645).

Visualization of droplet dynamics is provided by an inverted microscope (Nikon Ti-U) with a high-speed camera (Photron SA-5). The camera runs a 1024×1024 CMOS sensor with 20 μm square pixels and is capable of frame rates in excess of 1 Mfps at reduced spatial resolution. Image exposure is limited by the image

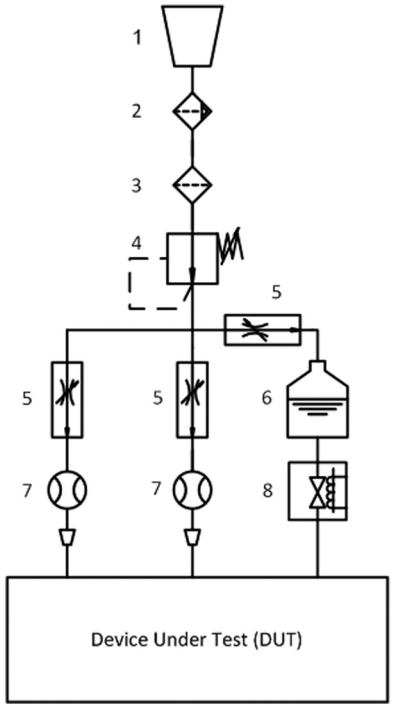

Fig. 4 Schematic of hardware and instruments for gas and liquid flow control: facility compressed air supply (1), desiccant dryer (2), submicron particulate filter (3), rough pressure regulator (4), pressure regulators with transducer feedback control (5), sealed liquid reservoir containing reactants to be mixed (6), mass flow sensors (7), miniature inert solenoid valve (8), and microfluidic device under test (DUT)

frame rate, but can be as low as 3 μs. The exposure time is ultimately determined by the light source used and degree of image contrast desired. When imaging in white light mode, such as that used for droplet this detachment study, the camera exposure can be arbitrarily small.

All pressure regulators, transducers, and flow meters were powered using dedicated 24 V DC power modules and activated through dedicated relay switches inside a data logger/switch unit (Agilent 34970A). The data logger also monitors flow rate and pressure data of the gas and liquid streams. The gas pressure regulators are controlled using a four channel DC power supply (HP 6627A). All power and data transmission cables are shielded and grounded. A dedicated host computer provides control, data acquisition, and real-time image visualization.

The spatial resolution of this experimental setup is determined by the microscope objective, the physical size of the camera imaging sensor, and the exposure time used to capture the images. The microscope objective used for these experiments provides an in-plane (diffraction limit) and out-of-plane (depth of field) spatial resolution of 0.67 and 3.4 μm, respectively. The physical size of each pixel on the imaging sensor is 20 μm, which, at 20× magnification, provides an in-plane spatial resolution of 1 μm. The exposure time controls how long the imaging sensor is gathering intensity data for each image. As the exposure duration is increased, the image intensity increases proportionally but highly dynamic events become blurred and difficult to resolve. The in-plane spatial resolution is therefore the product of the anticipated droplet velocity and exposure duration. For example, a droplet traveling at 1 m/s with an exposure of 1 μs provides an in-plane spatial resolution of 1 μm. The resulting in-plane spatial resolution of the measurement system is the maximum of these three sources. For the results presented in the following section, the in-plane spatial resolution ranged from 1 to 2 μm and was limited by the 20 μs exposure used for image capture.

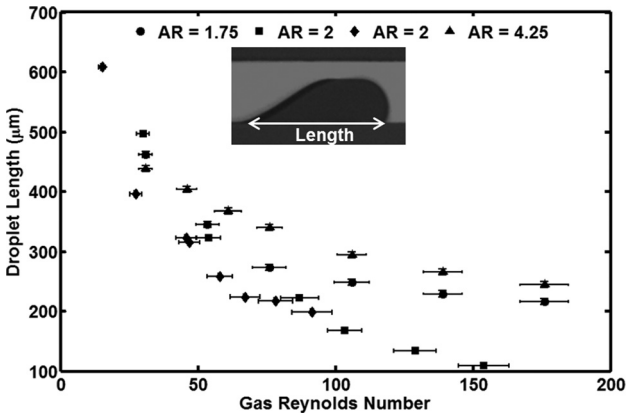

Fig. 5 Experimental data of detached droplet length versus air Reynolds number for three different channel aspect ratios and four different devices

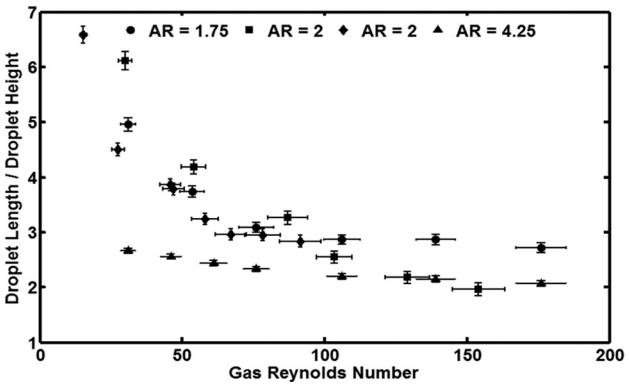

Fig. 7 Experimental data showing how the ratio of droplet length to height decreases with increasing air Reynolds number for three different channel aspect ratios and four different devices

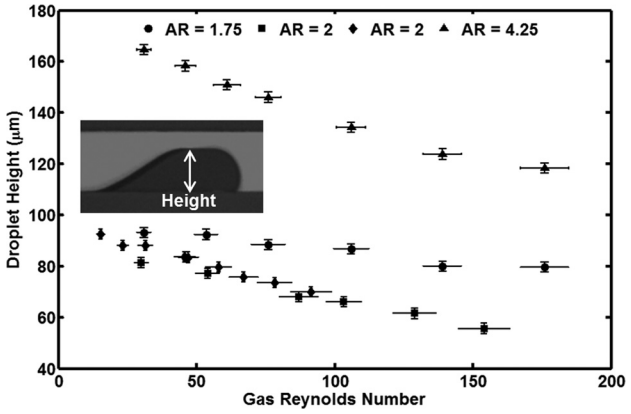

Fig. 6 Experimental data of detached droplet height versus air Reynolds number for three channel aspect ratios (channel height / channel depth) and four different devices

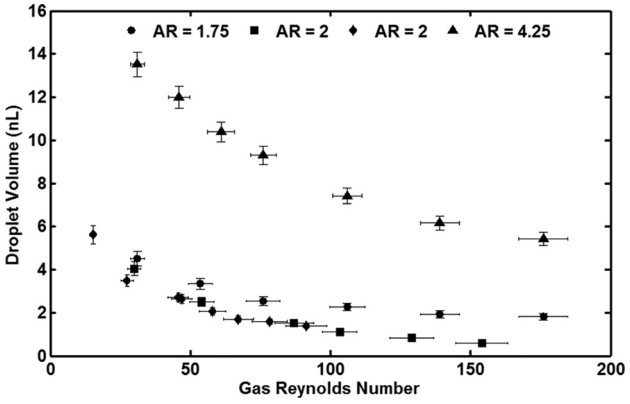

Fig. 8 Experimental data of detached droplet volume versus air Reynolds number for three different channel aspect ratios and four different devices

Experimental Results

The flow regime of interest in order to achieve the dripping regime using T-junction geometries ranges from $10 < \mathrm{Re}_{Dh} < 200$, where Re_{Dh} is the Reynolds number for air based on the average air velocity, channel hydraulic diameter, and air viscosity. This dynamic range should identify a transitional region where inertia supersedes viscous dominated detachment. Results of droplet height, length, and volume were obtained for four different microchannel devices and three different channel aspect ratios. The channel height and depth for each microchannel are $105 \times 59\ \mu$m, $100 \times 50\ \mu$m, $100 \times 50\ \mu$m, and $188 \times 44\ \mu$m with corresponding aspect ratios (*AR*) of 1.75, 2, 2, and 4.25, respectively. Figures 5 and 6 show detached droplet length and height for each experiment. Droplet height is confined by the height of the microchannel and therefore does not show as large of a change as compared to droplet length. Detached droplet aspect ratio, defined as droplet length over droplet height, is shown in Fig. 7. The microchannel with an aspect ratio of 4.25 consistently produced with the smallest aspect ratio. The detached droplet volume for each device is shown in Fig. 8. Note that droplet volume decreases with increasing Re_{Dh} for all cases considered. This implies that for a constant liquid injection rate, smaller droplets are produced at a higher rate. Droplet morphology is captured by the high speed images shown in Fig. 9, which are for a device with an aspect ratio of 2. As the Re_{Dh} increases, the detached shape transforms from a slug to a more spherical-like droplet. Note that the height of the droplet does not change as significantly as droplet length, as supported by

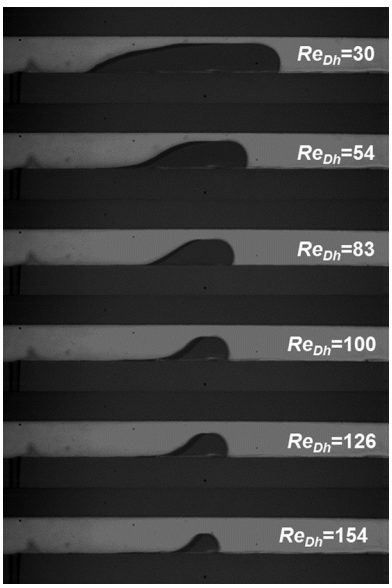

Fig. 9 High speed camera images of droplet geometry for different gas Reynolds numbers (Re_{Dh}) for a channel 100 μm high and 50 μm deep

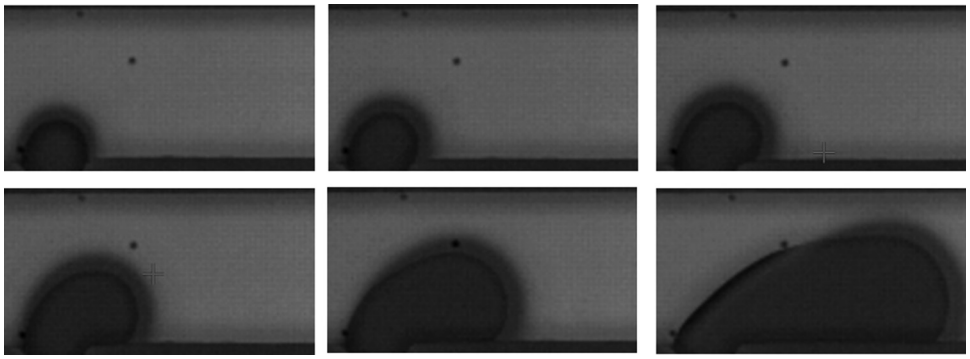

Fig. 10 High speed camera images of droplet growth and detachment for $Re_{Dh} = 118$

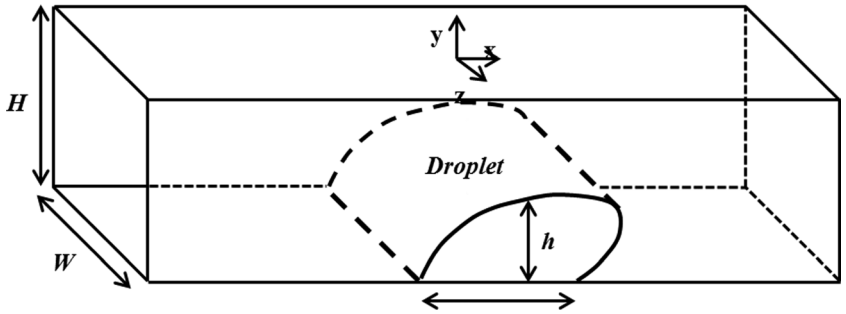

Fig. 11 Schematic of rectangular microchannel with a detached droplet/slug on the lower wall. The channel dimensions are: height, *H*, and depth, *W*. The droplet dimensions are height, *h*, and length, *l*. The Cartesian coordinate system used for the detachment analysis is also indicated.

the plots in Figs. 5 and 6. The detachment of a single droplet in a Re_{Dh} of 118 is shown by the images in Fig. 10. The droplet grows primarily in the lateral direction during the initial stages of detachment. Once the air flow is reduced, lateral growth gives way to longitudinal growth. The droplet continues growing in length until the surface tension pinning the droplet at the injection site is overcome by stresses induced by the high speed air flow.

Results and Discussion

To understand the dominant detachment mechanism in greater detail, a simple scaling analysis is presented that uses the detached height and length data. The schematic in Fig. 11 provides the relevant channel and droplet dimensions. By nondimensionalizing the measured droplet length by the channel hydraulic diameter, the data for each device collapses largely onto a single curve as shown by the plot in Fig. 12. This trend is consistent with previous measurements [19]. In contrast, the nondimensional droplet height shown in Fig. 13 does not show this behavior for large aspect ratios. Note that the nondimensional droplet height can exceed unity since the channel hydraulic diameter is less the channel height H for all devices tested.

The flow field of interest for droplet detachment is in the x–y plane. The initially fully developed flow must accelerate around the emerging droplet. Drag forces induced by the air flow compete with the surface tension force holding the droplet at the injection site. The sources of the drag force can be viscous, inertial, or hydrodynamic pressure difference. The viscous force shears the droplet while inertial drag pushes the droplet. The hydrodynamic pressure force results from the pressure drop as the air flows through the small gap between the top of the droplet and channel wall.

The dominant detachment mechanism can be verified by taking the ratio of the viscous, inertial, and hydrodynamic pressure forces to the surface tension force securing the droplet. A force ratio near unity indicates a balance between the detachment force and droplet pinning force. Assuming an x–y flow field with a negligible pressure gradient in the y-direction, the mass and x-direction momentum equations are:

$$\frac{\partial u}{\partial x} + \frac{\partial v}{\partial y} = 0 \tag{1}$$

$$\rho\left(u\frac{\partial u}{\partial x} + v\frac{\partial u}{\partial y}\right) = -\frac{dp}{dx} + \mu\left(\frac{\partial^2 u}{\partial x^2} + \frac{\partial^2 u}{\partial y^2}\right) \tag{2}$$

The air flow upstream of the droplet is fully developed but the flow in the narrow gap between the droplet and adjacent wall is not. Therefore, the inertia terms appearing on the left side of the momentum equation cannot be neglected. The terms on the right side of the momentum equation represent the force contributions due to axial pressure drop, normal viscous force, and tangential viscous force. The relative magnitudes of each term in the momentum equation can be quickly assessed by scaling arguments. The assumed velocity and length scales in the gap are as follows:

$$\begin{aligned} u &\sim U\frac{H}{(H-h)} \\ x &\sim l \\ y &\sim H - h \end{aligned} \tag{3}$$

In the above equation, U is the average velocity in the channel, H is the channel height, and l and h are droplet length and height, respectively. The y-velocity scale is found by scaling the mass conservation equation the known scales to yield

$$v \sim \frac{UH}{l} \tag{4}$$

Substituting these scales into the momentum equation yields the following:

$$\rho\left[\frac{\left(U\frac{H}{H-h}\right)^2}{l},\frac{\left(U\frac{H}{l}\right)\left(U\frac{H}{H-h}\right)}{H-h}\right]\sim\frac{\Delta p}{l},$$

$$\mu\left[\frac{U\frac{H}{H-h}}{l^2},\frac{U\frac{H}{H-h}}{(H-h)^2}\right]$$

$$\rho\frac{U^2}{l}\left(1-\frac{h}{H}\right)^{-2}\sim\frac{\Delta p}{l},\quad \mu\frac{U}{l^2}\left(1-\frac{h}{H}\right)^{-1},\quad \mu\frac{U}{H^2}\left(1-\frac{h}{H}\right)^{-3} \tag{5}$$

This result shows that both inertial terms are of the same magnitude. The dominating geometric parameter is clearly the ratio of droplet height to channel height. For this reason, the first viscous term can be neglected for channel aspect ratios near unity. To balance the forces occurring in the gap at the point of detachment, the surface tension pinning the droplet must be balanced by the inertial, viscous, and hydrodynamic pressure difference forces of the air flow. Intuitively, the long slug like droplets occurring at low Re_{Dh} suggests a shearing stress. The compact, small aspect ratio droplets detached at higher Re_{Dh} conversely suggest inertial and hydrostatic pressure balancing. By taking the ratio of the surface tension pinning force to the air inertial, viscous, and hydrodynamic pressure forces, the detachment mechanism may be revealed.

During the growth process, the droplet wets the channel walls and remains attached to the surface. The force per unity length securing the droplet to the injection site is

$$F'_P=\sigma\cos(\theta_R-\theta_A) \tag{6}$$

The angles in parentheses, θ_R and θ_A, are the receding and advancing droplet contact angles. These are readily evident in the images shown in Fig. 9 and range from $30\,\mathrm{deg}<\theta_R<40\,\mathrm{deg}$ and $100\,\mathrm{deg}<\theta_A<110\,\mathrm{deg}$. This force acts along the contact line of the droplet and channel wall.

Conventional nondimensional parameters that are used in microchannel liquid flows are the Capillary (Ca) number and Weber (We) number. The Ca number assesses the dominance of the viscous forces at the droplet interface to the surface tension forces. A value of unity implies these forces are balanced. The We number relates the dominance of the droplet inertia to the droplet surface tension. For the detachment process, it makes more sense to relate the viscous stress induced by and the inertia carried by the high speed air flow to the surface tension of the droplet for the Ca and We number, respectively. This type of ratio may be more applicable since both phases are included. A Ca number greater than unity implies the air subjects larger viscous forces on the droplet compared to the droplet surface tension force. The viscous stress in this case is due to the squeezed air flow in the narrow gap. Similarly, a We number greater than unity suggests the air imposes a greater inertial force in comparison to the droplet surface tension force. The inertia in this case is due to the air flow upstream of the droplet. If the modified Capillary number or modified Weber numbers exceed unity, the droplet should detach. The mechanism for detachment, however, is different.

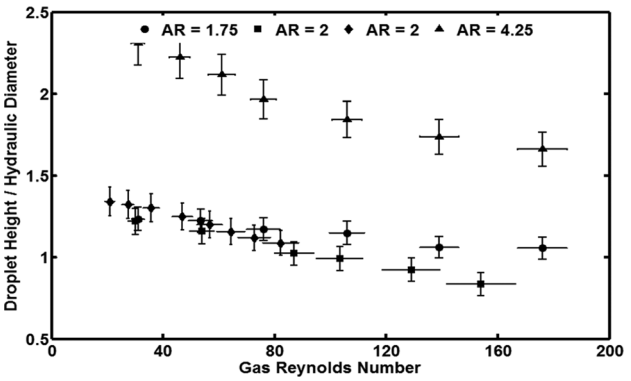

Fig. 13 Experimental data of detached droplet height versus air Reynolds number for three different channel aspect ratios and four different devices. Data has been nondimensionalized by channel hydraulic diameter. Note that the droplet height ratio can exceed unit using this nondimensionalization.

Based on the measured gas flow rates, channel dimensions, and droplet length and height, the modified dimensionless parameters that access the contributions of gas phase inertial changes, viscous stresses, and hydrodynamic pressure differences are determined. The ratio of the inertial force of the gas to the surface tension pinning force gives a modified Weber ($\mathrm{We}_{\mathrm{Mod}}$) number

$$\mathrm{We}_{\mathrm{Mod}}=\frac{\rho U^2\left(\frac{H}{H-h}\right)^2 hW}{\sigma\cos(\theta_R-\theta_A)(W+2h)} \tag{7}$$

$\mathrm{We}_{\mathrm{Mod}}$ is plotted against Re_{Dh} in Fig. 14. This ratio is greater than unity for all channel aspect ratios considered past a Re_{Dh} of 50.

The ratio of the viscous force imposed by the gas to the surface tension pinning force gives a modified Capillary ($\mathrm{Ca}_{\mathrm{Mod}}$) number:

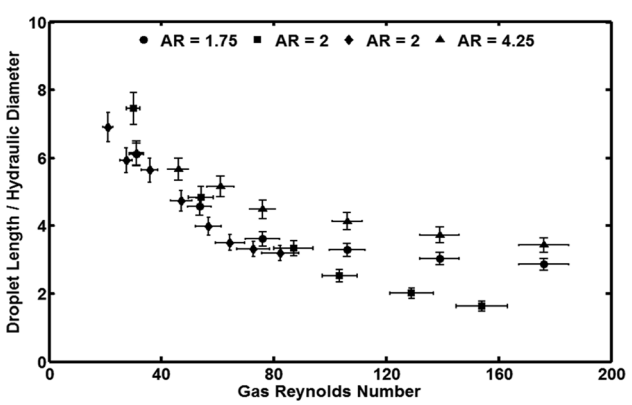

Fig. 12 Experimental data of detached droplet length versus air Reynolds number for three different channel aspect ratios and four different devices. Data has been nondimensionalized by channel hydraulic diameter.

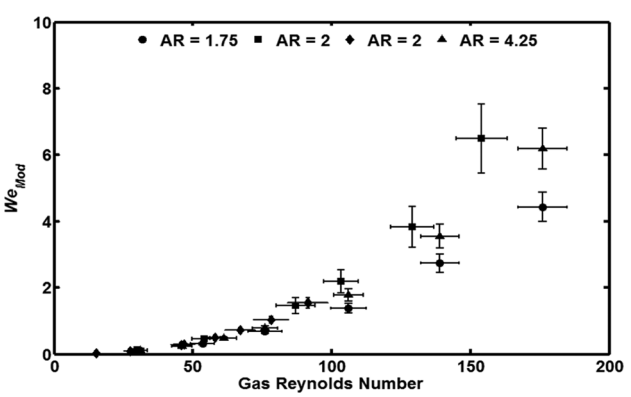

Fig. 14 Plot showing how the ratio of gas-phase inertial force to droplet surface tension, $\mathrm{We}_{\mathrm{Mod}}$, changes with increasing Re_{Dh}. The ratio exceeds unity past a Re_{Dh} 80 and indicates a transition to inertial droplet detachment.

$$\mathrm{Ca}_{\mathrm{Mod}} = \frac{\mu U\left(\frac{H}{H-h}\right)\frac{lW}{H-h}}{\sigma\cos(\theta_R - \theta_A)(W+2h)} \tag{8}$$

Data for $\mathrm{Ca}_{\mathrm{Mod}}$ across the range of Re_{Dh} is shown in Fig. 15. At low Re_{Dh}, $\mathrm{Ca}_{\mathrm{Mod}}$ is of order unity and decays as Re_{Dh} increases. The exception is the channel with the smallest aspect ratio, which remains above 1 across the flow range considered. However, $\mathrm{Ca}_{\mathrm{Mod}}$ is less than $\mathrm{We}_{\mathrm{Mod}}$ for all tested devices once a Re_{Dh} of 60 is exceeded. This indicates a transition from viscous dominated drag to inertial drag.

The last force of interest is the pressure difference that results due to viscous losses and inertial gains in the narrow gap. The result is a net pressure force acting in the flow direction. Assuming a fully developed flow, the pressure through the gap is estimated as

$$\Delta p = f\frac{l}{D_{h,\mathrm{Gap}}}\frac{1}{2}\rho U_{\mathrm{Gap}}^2 \tag{9}$$

The value of the friction factor f depends on the shape of the channel cross-section. For a round tube, $f\,\mathrm{Re}_{Dh}$ is 64 while for a duct of infinite depth it is 96. A duct with an aspect ratio of 4 gives an $f\,\mathrm{Re}_{Dh}$ of ~73. The gap aspect ratio (gap height/channel depth) for these tests was approximately 1.5 for all devices except for the 4.25 aspect ratio channel, which showed a gap aspect ratio of approximately 3. The $f\,\mathrm{Re}_{Dh}$ used for this analysis was 57 for $AR = 1.75$–2 and 73 for $AR = 4.25$. The ratio of pressure to surface tension forces is then

$$\frac{\text{Pressure force}}{\text{Surface tension force}} = \frac{f\frac{l}{D_{h,\mathrm{Gap}}}\rho U^2\left(\frac{H}{H-h}\right)^2 hW}{\sigma\cos(\theta_R - \theta_A)(W+2h)} \tag{10}$$

The pressure force to surface tension ratio for the range of Re_{Dh} tested is shown in Fig. 16. The important thing to note here is that this ratio is larger than unity for all detached droplets but decreases as Re_{Dh} increases much like $\mathrm{Ca}_{\mathrm{Mod}}$. This indicates that the dominant detachment mechanism at low Re_{Dh} is the hydrodynamic pressure difference but transitions to inertial drag detachment as Re_{Dh} increases. This is captured by the plot in Fig. 17, which shows the inertia and pressure detachment ratios for the $100 \times 50\,\mu$m microchannel. The transition from pressure to inertial detachment occurs near Re_{Dh} of 100.

It is also apparent from the flow regime picture inlays that when the hydrostatic pressure difference is the dominant detachment mechanism ($\mathrm{Re}_{Dh} < 100$), the liquid droplets detach as long slugs of decreasing length with Re_{Dh}. On the other hand, when the inertial drag force becomes the primary detachment mechanisms, the droplets become more spherical during detachment and uniformly decrease in size with Re_{Dh}. The reason for this change in droplet geometry with detachment mechanism transition is directly related to the forces involved in the process.

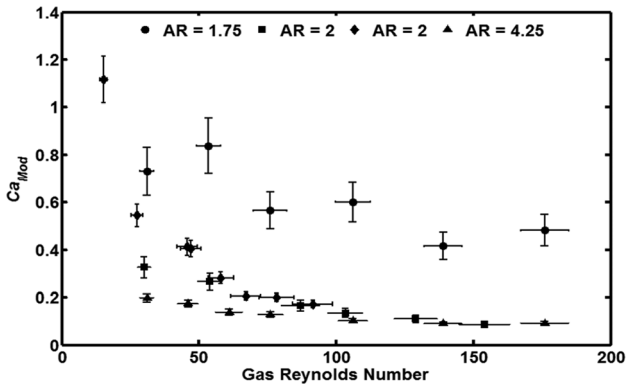

Fig. 15 Plot showing how the ratio of the imposed gas-phase viscous force to droplet surface tension, $\mathrm{Ca}_{\mathrm{Mod}}$, changes with increasing Re_{Dh}. The ratio is less than unity for all channel aspect ratios considered.

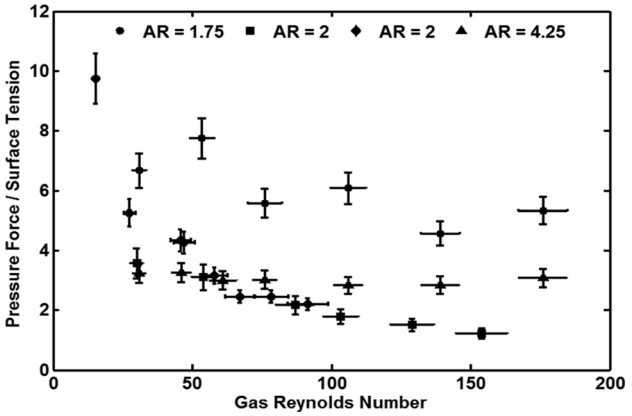

Fig. 16 Plot showing how the ratio of pressure drop across the droplet to the surface tension securing the droplet at the injection site changes with increasing Re_{Dh}. The ratio is largest for the channel with the smallest aspect ratio and decreases for all channel sizes with increasing Re_{Dh}.

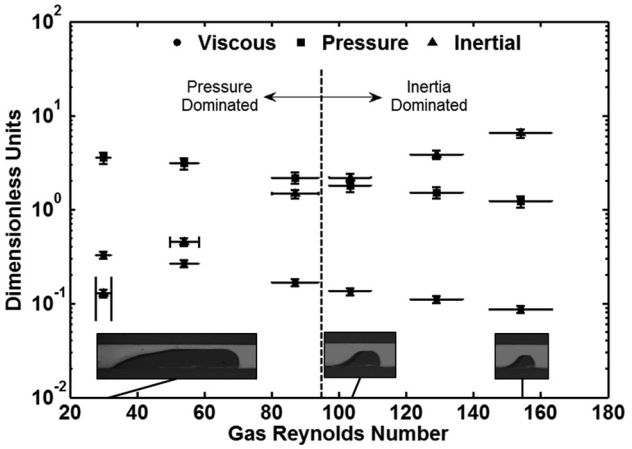

Fig. 17 Comparison of experimental data showing the viscous, pressure, and inertial detachment ratios for the $100 \times 50\,\mu$m channel. The detachment mechanism transitions from pressure to inertial near Re_{Dh} of 100. The still images of detached droplets shown in the lower portion of the figure were captured at the indicated Reynolds number indicated and clearly show how droplet shape transitions from elongated slugs to more spherical droplets with increasing gas-phase inertia.

Since the hydrodynamic pressure difference force is viscous in nature, it scales linearly with microchannel air velocity U and inversely with gap height H–h. Therefore, there is really no reason for the droplet slug height h to substantially decrease with increasing microchannel air velocity U, as these two effects would counteract each other in terms of the hydrodynamic pressure difference established in the gap region. Thus, with a constant gap height an increase of the microchannel air velocity will lead to a higher hydrodynamic pressure force. Since it was already established that there is no incentive for the droplet slug height to chance, the surface tension force remains the same and in order to balance the higher hydrostatic pressure gradient, a shorter slug length is required that produce the same net pressure drop force.

Conversely, the inertial drag force scales as the square of the microchannel air velocity and is not dependent on the gap height

or droplet length—only its cross-sectional area. Thus, as the microchannel air velocity increases, the droplet is bound to decrease more rapidly in size to counteract this increase in dynamic pressure (droplet cross sectional area is inversely proportional to U^2). This decrease in droplet size is somewhat softened by the fact that the pinning surface tension force is also proportional to droplet height through interaction from the side walls.

Conclusion

The understanding of liquid droplet detachment in high speed, confined, microchannel gas flows is critical in the realization of an inertia-based micromixer. This paper presented experimental results of water droplet detachment in an air flow where the droplet height and length was measured across a range of air Reynolds numbers and for different microchannel aspect ratios. The objective was to determine the droplet detachment mechanism when the inertia of the continuous phase is increased. The results indicate that the detached droplet transitions from an elongated slug at low Reynolds numbers to a nearly uniform aspect ratio droplet at high Reynolds numbers. The mechanism leading to detachment was investigated by using simple scaling arguments based on the forces induced by the gas on the liquid with particular attention given to the reduced flow area between the droplet and adjacent microchannel at the time of detachment. The surface tension pinning the droplet at the injection site was compared to inertial, viscous, and hydrostatic forces induced by the air flow. These modified dimensionless parameters indicated that the dominate droplet detachment mechanism transitions from hydrostatic to inertial origins for an air Reynolds number near 100. Although viscous losses in the gap contribute to the resulting pressure drop across the droplet, viscous forces alone are not sufficient to overcome the surface tension forces at the injection site.

These results suggest that low Reynolds number (<100) gas flows must be used when a liquid-gas plug flow train is desired, such as in heterogeneous catalysis continuous flow microreactors. This upper bound on the Reynolds number required to allow slug formation puts limits on the maximum flow rates that can be achieved on these systems. On the other hand, when isolated or monodisperse droplets are required, as is the case in sprays and aerosols, higher Reynolds number (>100) inertial detachment is desired. These findings are also invaluable when designing droplet collision micromixers where droplet aspect ratio and droplet velocity are critical parameters. They support the trends of reduced mixing times with increased continuous phase Reynolds number. The higher droplet collision speeds achieved under these conditions and their corresponding smaller dimensions lead to substantial decreases in mixing times.

One important operation of any droplet-based micromixer that has not been addressed by this work is droplet generation frequency. The over-arching objective of this effort was an understanding of how a continuous liquid stream is discretized into droplets and slugs by virtue of a cross-flowing gaseous stream. As such, developing a parameter space that includes droplet generation rates was beyond the scope. The next logical step in realizing the potential advantages of gas-liquid microfluidic architectures is the formulation of how both gas and liquid flow regimes affect droplet generation rates and ultimately product throughput.

Acknowledgment

This work was supported by DARPA 2008 Young Faculty Award (YFA) Grant No. HR0011-08-1-0045.

Nomenclature

$\mathrm{Ca}_{\mathrm{Mod}}$ = modified Capillary number, dimensionless
f = Darcy friction factor, dimensionless
H = channel height, m
h = droplet height, m
l = characteristic droplet length scale, m
Δp = pressure difference, $\mathrm{N\,m^{-2}}$
Re = Reynolds number, dimensionless
Re_{Dh} = Reynolds number based on channel hydraulic diameter, dimensionless
u = x-direction velocity, $\mathrm{m\,s^{-1}}$
U = mean velocity in channel, $\mathrm{m\,s^{-1}}$
v = y-direction velocity, $\mathrm{m\,s^{-1}}$
W = channel depth into page, m
We = Weber number, dimensionless
$\mathrm{We}_{\mathrm{Mod}}$ = modified Weber number, dimensionless
x = Cartesian coordinate direction
y = Cartesian coordinate direction
z = Cartesian coordinate direction

Greek Symbols

μ = fluid dynamic viscosity, $\mathrm{kg\,m^{-1}\,s^{-1}}$
θ_A = advancing contact angle, degrees
θ_R = receding contact angle, degrees
ρ = density, $\mathrm{kg\,m^{-3}}$
σ = surface tension, $\mathrm{J\,m^{-2}}$

References

[1] Bui, A., and Zhu, Y., 2007, "Numerical Study of Droplet Generation in a Complex Micro-Channel," Proceedings of the 16th Australasian Fluid Mechanics Conference, Gold Coast, Australia.
[2] van der Graaf, S., Steegmans, M., van der Sman, R. G. M., Schroen C. G. P. H., and Boom, R. M., 2005, "Droplet Formation in a T-Shaped Microchannel Junction: A Model System for Membrane Emulsification," Colloids Surf., A, **266**, pp. 106–116.
[3] van der Graaf, S., Nisisako, T., Schroen, C. G. P. H., van der Sman, R. G. M., and Boom, R., 2006, "Lattice Boltzmann Simulations of Droplet Formation in a T-Shaped Microchannel," Langmuir, **22**, pp. 4144–4152.
[4] Liu, H., and Zhang, Y., 2009, "Droplet Formation in a T-Shaped Microfluidic Junction," J. Appl. Phys., **106**, p. 034906.
[5] Plateau, J., 1873, "Experimental and Theoretical Statistics of Liquids Subject to Molecular Forces Only," Mem. Acad. R. Sci. Fr., **1**, pp. 4–24.
[6] Savart, F., 1833, "Memoire Sure le Choc D'une Veine Liquid Lancee Contre un Plan Circulair," Ann. Chim. Phys., **54**, pp. 54–87.
[7] Rayleigh, L., 1878, "On the Instability of Jets," Proc. London Math. Soc., **10**(4), pp. 4–13.
[8] Rayleigh, L., 1879, "On the Capillary Phenomena of Jets," Proc. R. Soc. London, **29**, pp. 71–97.
[9] Bogy, D. B., 1979, "Drop Formation in a Circular Liquid Jet," Ann. Rev. Fluid Mech., **11**, pp. 207–228.
[10] Qian, J., and Law C. K., 1997, "Regimes of Coalescence and Separation in Droplet Collision," J. Fluid Mech., **331**(1), pp. 59–80.
[11] Orme, M., 1997, "Experiments on Droplet Collisions, Bounce, Coalescence and Disruption," Prog. Energy Combust. Sci., **23**(1), pp. 65–79.
[12] Simpson, S. F., Kincaid, J. R., and Holler F. J., 1983, "Microdroplet Mixing for Rapid Reaction Kinetics With Raman Spectrometric Detection," Anal. Chem., **55**(8), pp. 1420–1422.
[13] Wang, F.-C., Feng J.-T., and Zhao Y.-P., 2008, "The Head-On Colliding Process of Binary Liquid Droplets at Low Velocity: High-Speed Photography Experiments and Modeling," J. Colloid Interface Sci., **326**(1), pp. 196–200.
[14] Aryafar, H., and Kavehpour, H. P., 2006, "Drop Coalescence Through Planar Surfaces," Phys. Fluids, **18**(7), p. 072105.
[15] Christopher, G. F., Bergstein, J., End, N. B., Poon, M., Nguyen, C., and Anna S. L., 2009, "Coalescence and Splitting of Confined Droplets at Microfluidic Junctions," Lab Chip, **9**(8), pp. 1102–1109.
[16] Zhu, X., Sui, P., and Djilali, N., 2008, "Numerical Simulation of Emergence of a Water Droplet from a Pore into a Microchannel Gas Stream," Microfluid. Nanofluid., **4**(6), pp. 543–555.
[17] Carroll, B., and Hidrovo, C., 2009, "An Experimental Investigation of Droplet Detachment in High-Speed Microchannel Air Flow," Proceedings of the 2nd ASME Micro/Nanoscale Heat & Mass Transfer International Conference, Shanghai, PRC, Vol. 1, pp. 289–298.
[18] Sugiura, S., Nakajima, M., and Seki M., 2002, "Prediction of Droplet Diameter for Microchannel Emulsification," Langmuir, **18**(10), pp. 3854–3859.
[19] Hidrovo, C. H., Wang, F. M., Steinbrenner, J. E., Lee, E. S., Vigneron, S., Cheng, C. H., Eaton, J. K., and Goodson, K. E., 2005, "Water Slug Detachment in Two-Phase Hydrophobic Microchannel Flows," Proceedings of the ASME 3rd International Conference on Microchannels and Minichannels, pp. 709–715.
[20] Christopher, G., and Anna S., 2007, "Microfluidic Methods for Generating Continuous Droplet Streams," J. Phys. D: Appl. Phys., **40**, pp. 319–336.
[21] Xiang, Y., and LaVan, D., 2009, "Droplet Formation at Microfluidic T-Junctions," Mater. Res. Soc. Symp. Proc., **1139**.